Journal of Science and Technology - Smart Systems and Devices
Volume 36, Issue 3, May 2026, 001–012

Hybrid Backstepping and Fast Terminal Sliding Mode Control for Balancing of Two-Wheeled Mobile Robots

Hoang-Tung Nguyen, Duc-Manh Nguyen, Bac-Ky Ha, Thi-Van-Anh Nguyen, Manh-Linh Nguyen*

Hanoi University of Science and Technology, Hanoi, Vietnam
**Corresponding author email: linh.nguyenmanh@hust.edu.vn*

Abstract

This paper proposes a two-layer fast terminal sliding mode controller (FTSMC) combined with a conventional sliding mode control (SMC) to achieve both trajectory tracking and balance control for a two-wheeled balancing mobile robot (TWBMB). First, the modeling procedure of the is examined using the Lagrangian approach, and the trajectory tracking error is formulated in the global coordinate system. Next, for trajectory tracking, the linear and angular velocities are controlled using a backstepping controller. Two SMCs are employed to regulate the wheel torque, ensuring balance and convergence of velocity to the backstepping reference: the two-layer FTSMC is responsible for velocity and balancing while the conventional SMC manages tilt angle. Simulation results verify the fast response and superior velocity tracking, as well as the self-balancing performance of the developed controller.

Keywords: Fast Terminal Sliding mode control, Stability control, Trajectory tracking, Two-wheeled balancing mobile robots.

1. Introduction

In recent years, wheeled mobile robots (WMRs) [1] have garnered significant research interest due to their extensive range of applications: transportation [2], agriculture [3], delivery [4], home services [5], surveillance [6]. Performing these tasks highly depends on perception, navigation, and control. The Two-Wheeled Balancing Mobile Robot (TWBMR) is a common type of Wheeled Mobile Robot (WMR), which is inspired by the dynamics of the inverted pendulum. TWBMR is characterized by its lightweight design, compact footprint, rapid rotation, and exceptional agility, making it highly efficient for applications in transportation and surveillance, particularly in dynamic environments with numerous moving objects, such as parks and factories.

TWBMR comprises dual side-by-side wheels mounted on a common axis and a body that encases the system hardware. The TWBMR utilizes its two independently driven wheels to achieve self-stabilization, perform precise motion control, and operate effectively in dynamic environments. The operating mode of the TWBRM is based on controlling the robot's center of gravity, with its balance achieved through body inclination and the movement of the two wheels. It is also an inherently unstable system due to its configuration with only two support points, two motors for each wheel, and the ability to move freely in both position and tilt. From an automatic control perspective, the TWBMR is characterized as a nonlinear, dynamically complex, underactuated, and strongly coupled system. Modeling and control of TWBMRs have been studied in [7]. In several research works, linear state feedback strategies have been adopted to regulate the behavior of the linearized model. Recent studies have also investigated classical control schemes such as LQR optimized via metaheuristic algorithms for two-wheeled balancing robots, reporting improved performance compared to conventional tuning methods [8]. However, such approaches often involve increased computational complexity and rely on offline optimization procedures, which may limit their applicability in real-time implementations. A linear robust control approach for the TWBMR system was proposed in [9]. Excluding the yaw angle from the controller design, the feedback linearization approach has been utilized for the control and stabilization of TWBMR in [10]. These linear model-based designs neglect certain nonlinearities of the TWBMR system, resulting in discrepancies between the actual system behavior and the nominal model. Knowledge-based control approaches, such as fuzzy control, which derive the controller directly from the nonlinear system dynamics, have attracted considerable attention [11], [12]. Fuzzy systems are regarded as effective tools in robotic control and applications, enabling the handling of mathematically complex systems under various uncertainties [13]. However, developing fuzzy controllers demands significant expertise to define suitable membership

p-ISSN 3093-3285
e-ISSN 3093-3315
https://doi.org/10.51316/jst.xxx.ssad.2026.36.2.1
Received: Oct 18, 2025; Revised: Feb 25, 2026;
Accepted: Apr 12, 2026; Online:. May 28, 2026

functions. The lack of a structured method for specifying membership parameters complicates the design and implementation of fuzzy controllers. studies have attempted to enhance fuzzy-based control frameworks by integrating advanced optimization or adaptive mechanisms to improve performance and robustness in robotic systems [14]. Nevertheless, such approaches often introduce additional design complexity and computational burden, particularly when applied to real-time control of nonlinear and underactuated robots. Other intelligent methods, such as learning algorithms, struggle to perform effectively under external disturbances because of their long training times. The controller for a TWBMR must rebalance the robot when an imbalance occurs. In addition to model-based control approaches, observer-based control strategies have been investigated to cope with unmeasured states and unknown disturbances in two-wheeled inverted robots. In particular, Tran et al. proposed observer-based controllers that estimate system states and lumped disturbances, thereby improving robustness without requiring full-state measurements [15, 16].

Sliding Mode Control (SMC) is another control technique widely applied in robotic control applications [17]. SMC is widely recognized for its fast response and robustness against disturbances and uncertainties. The core principle of this method is to drive the system states toward a specified sliding manifold and maintain them on it thereafter. A discrete-time SMC approach addressing the path-following problem of wheeled mobile robots was introduced in [18]. To enhance the convergence rate of the system states toward the sliding surface, numerous modifications have been proposed. The terminal sliding mode control (TSMC) approach was introduced to ensure rapid convergence within a finite time [19]; however, it exhibits slow convergence near the equilibrium point. Subsequently, the fast terminal sliding mode control (FTSMC) approach was developed to enhance convergence speed relative to TSMC [20]. In [21], an SMC approach was proposed to control underactuated mechanical systems. The backstepping approach applied to the kinematic controller is a widely used method for WMR control [22]. In this technique, a series of intermediate control laws are introduced for specific system outputs. Subsequently, an additional control strategy is employed to implement these virtual control laws and achieve the desired system behavior.

This study proposes a backstepping technique for the kinematic model, followed by a hybrid controller that combines a two-layer fast terminal sliding mode control (FTSMC) and conventional sliding mode control (SMC) to improve the stability and tracking accuracy of the TWBMR system. Accordingly, the mathematical model of the TWBMR is established using the Lagrangian formulation.

The rest of this paper is organized as follows: Section 2 presents the system dynamic modeling, Section 3 details the design of the control structure based on the dynamic model, and Section 4 provides the simulation results obtained using MATLAB. Finally, the conclusion provides a summary of the study and its key findings.

2. Modeling

The modeling of a TWBMR is divided into 2 parts: kinematic and dynamic modeling. Kinematic modeling characterizes the system by establishing the geometric relationships and the mathematical formulation of motion, without taking into account the effects of mass, inertia, or external forces. Dynamic modeling investigates system behavior with considering the effects of forces, moments, and energy interactions that are directly related to the chassis.

The TWBMR system, modeled as an inverted pendulum, is shown in Fig.1, where the chassis is fitted with two individually driven wheels. The schematic diagram defines three coordinate systems: $\{M\}$ with axes (m_1, m_2, m_3), located at the midpoint of the wheel axis; $\{B\}$ with axes (b_1, b_2, b_3), positioned at the pendulum's center of mass; and $\{N\}$ with axes (n_1, n_2, n_3), fixed to the ground.

In Fig.1 , D represents the distance between the two wheels, R denotes the wheel radius, and L corresponds to the length of the inverted pendulum of the TWBMR. The mass of the pendulum (excluding the wheels) is denoted by m_p, while the mass of each wheel is represented by m_w. The moments of inertia of the pendulum about its mass center along the three principal coordinate axes are denoted by I_a, I_b, I_c. In addition, J and K represent the wheel's rotational inertias around the vertical axis passing through the wheel hub and around the axis orthogonal to it.

The subscripts used in the following notation indicate the respective components: left wheel (L), right wheel (R), wheel-axis midpoint (M), and pendulum body (B). Exponents are used to indicate the reference coordinate, with the inertial coordinate N written without a symbol. The main parameters are defined as follows: Ω_L, Ω_R, Ω_P represent the rotational speed vectors of the left wheel, right wheel, and pendulum; V_L, V_R, V_P correspond to the linear speed vectors of their mass centers; x_c, y_c, z_c specify the location of the system's central point in coordinate $\{N\}$. V^M and ω^M represent the linear and angular velocities of the 2TWBMR in coordinate $\{M\}$. T_L and T_R correspond to the wheel torques; γ_L and γ_R are the wheel rotation angles; $\dot{X}$, $\dot{\alpha}$, $\dot{\beta}$ denote the longitudinal velocity, angular rate around the pitch axis, and angular rate around the yaw axis; f_L and f_R represent the frictional torques acting on the left and right wheels.

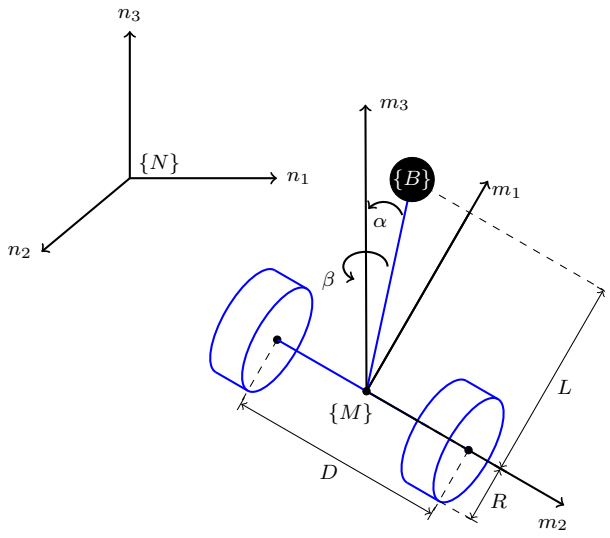

Fig. 1. TWBMR based on inverted pendulum

2.1. Kinematic Modeling

The TWBMR system is characterized by six generalized coordinates.

$$p = \begin{bmatrix} x_c & y_c & \beta & \alpha & \gamma_r & \gamma_l \end{bmatrix}^T \tag{1}$$

where γ_r and γ_l represent the rotation angles of the right and left wheels.
The motion of each body's center of mass is subject to the following holonomic constraints:

$$\begin{aligned} x_b &= x_C + L\sin\alpha\cos\beta \\ y_b &= y_C + L\sin\alpha\sin\beta \\ z_b &= z_C + L\cos\alpha \\ x_l &= x_C - \frac{D}{2}\sin\beta \\ y_l &= y_C + \frac{D}{2}\cos\beta \\ x_r &= x_C + \frac{D}{2}\sin\beta \\ y_r &= y_C - \frac{D}{2}\cos\beta \end{aligned} \tag{2}$$

It is assumed that the TWBMR moves under the conditions of pure rolling without lateral slip, which can be expressed through the following nonholonomic constraint:

$$\dot{y}_c\cos\beta - \dot{x}_c\sin\beta = 0 \tag{3}$$

The translational velocity along the axis (V_{xr}) and the angular velocity are expressed as:

$$V_{xr} = \frac{R}{2}(\dot{\gamma}_r + \dot{\gamma}_l) \tag{4}$$

$$\dot{\beta} = \frac{R}{D}(\dot{\gamma}_r - \dot{\gamma}_l) \tag{5}$$

The connection between the Cartesian velocities ($\dot{x}_c$) and ($\dot{y}c$) and the robot's translational velocity (Vxr) is expressed as:

$$\dot{x}_c = V_{xr}\cos\beta \tag{6}$$

$$\dot{y}_c = V_{xr}\sin\beta \tag{7}$$

From equations (4) to (7), two more nonholonomic constraints can be derived:

$$\dot{y}_c\sin\beta - \dot{x}_c\cos\beta = R\dot{\gamma}_l + \frac{D}{2}\dot{\beta} \tag{8}$$

$$\dot{y}_c\sin\beta - \dot{x}_c\cos\beta = R\dot{\gamma}_r - \frac{D}{2}\dot{\beta} \tag{9}$$

The kinematic constraints in (3), (8), (9) are expressed as follows:

$$\mathbf{A}(\mathbf{p})\dot{\mathbf{p}} = 0 \tag{10}$$

where

$$\mathbf{A}(\mathbf{p}) = \begin{bmatrix} -\sin\beta & \cos\beta & 0 & 0 & 0 & 0 \\ \cos\beta & \sin\beta & \frac{D}{2} & 0 & -R & 0 \\ \cos\beta & \sin\beta & \frac{D}{2} & 0 & 0 & -R \end{bmatrix} \tag{11}$$

2.2. Dynamic Modeling

The velocities of components L, R, B relative to the $\{N\}$ reference coordinate are obtained by taking the derivative of equation (2), yielding the following expressions:

$$V_L = \left(x_C - \frac{D}{2}\dot{\beta}\cos\beta\right)n_1 + \left(y_C - \frac{D}{2}\dot{\beta}\sin\beta\right)n_2 \tag{12}$$

$$V_R = \left(x_C + \frac{D}{2}\dot{\beta}\cos\beta\right)n_1 + \left(y_C + \frac{D}{2}\dot{\beta}\sin\beta\right)n_2 \tag{13}$$

$$\begin{aligned} V_P = {} & \left(x_C + L\dot{\alpha}\cos\alpha\cos\beta - L\dot{\beta}\sin\alpha\sin\beta\right)n_1 \\ & + \left(\dot{y}_C + L\dot{\alpha}\cos\alpha\sin\beta - L\dot{\beta}\sin\alpha\cos\beta\right)n_2 \\ & - L\dot{\alpha}\sin\alpha\, n_3 \end{aligned} \tag{14}$$

The rotational motion of the components $\{L, R, B\}$ is described by the following angular velocity equations:

$$\Omega_L = \Omega^M + \dot{\gamma}_L m_2 = \dot{\beta}m_3 + \left(\frac{1}{R}\right)\left(x - \frac{D}{2}\dot{\beta}\right)m_2 \tag{15}$$

$$\Omega_R = \Omega^M + \dot{\gamma}_R m_2 = \dot{\beta}m_3 + \left(\frac{1}{R}\right)\left(x + \frac{D}{2}\dot{\beta}\right)m_2 \tag{16}$$

$$\Omega_P = \Omega^M + \dot{\alpha}b_2 = (-\dot{\beta}\sin\alpha)b_1 + \dot{\alpha}b_2 + (\dot{\beta}\cos\alpha)b_3 \tag{17}$$

The overall kinetic energy of the TWBMR, encompassing both linear and rotational motion, is expressed as:

$$\begin{aligned} T_1 = {} & \frac{1}{2}m_w(V_L)^T V_L + \frac{1}{2}m_w(V_R)^T V_R \\ & + \frac{1}{2}m_P(V_P)^T V_P \end{aligned} \tag{18}$$

$$T_2 = \frac{1}{2}(\Omega_L)^T I_L \Omega_L + \frac{1}{2}(\Omega_R)^T I_R \Omega_R + \frac{1}{2}(\Omega_P)^T I_P \Omega_P \quad (19)$$

where I_L, I_R, I_P are inertia matrices of three bodies:

$$I_L = I_R = diag\{K, J, K\} \quad (20)$$

$$I_P = diag\{I_A, I_B, I_C\} \quad (21)$$

The potential energy of the TWBMR, considering its movement on a flat surface, is given by:

$$U = m_p g L \cos\alpha \quad (22)$$

The Lagrangian is formulated as:

$$L = T - U = T_1 + T_2 - U \quad (23)$$

Applying Lagrange's equation yields:

$$\frac{d}{dt}\left(\frac{\partial L}{\partial \dot{\mathbf{p}}}\right) - \frac{\partial L}{\partial \mathbf{p}} = \boldsymbol{\phi} + \mathbf{A}(\mathbf{p})^T \boldsymbol{\lambda} \quad (24)$$

where $\boldsymbol{\lambda}$ represents the Lagrange multiplier and $\boldsymbol{\phi}$ denotes the vector of external forces associated with the six coordinates:

$$\boldsymbol{\phi} = \begin{bmatrix} 0 \\ 0 \\ 0 \\ T_L + T_R - c(\dot{\gamma}_L - \dot{\alpha}) - c(\dot{\gamma}_R - \dot{\alpha}) \\ T_R - c(\dot{\gamma}_R - \dot{\alpha}) \\ T_L - c(\dot{\gamma}_L - \dot{\alpha}) \end{bmatrix} \quad (25)$$

where c represents the viscous damping coefficient acting on the wheel axis.
Solving the Lagrangian equation without the Lagrange multipliers, the dynamic equations can be represented as:

$$M\ddot{q} + C\dot{q} + H\dot{q} + G = B\tau \quad (26)$$

Where the system's velocity vector is given by

$$\dot{q} = [V_{xr}; \dot{\alpha}; \dot{\beta}]^T \quad (27)$$

and M denotes the inertia matrix, C represents the Coriolis and centrifugal force matrix, H is the friction matrix, B is the input matrix, and τ indicates torque matrix;

$$M = \begin{bmatrix} a_{11} & a_{12} & 0 \\ a_{21} & a_{22} & 0 \\ 0 & 0 & a_{33} \end{bmatrix}; \quad C = \begin{bmatrix} 0 & c_{12} & c_{13} \\ 0 & 0 & c_{23} \\ c_{31} & c_{32} & c_{33} \end{bmatrix}$$

$$G = \begin{bmatrix} 0 \\ -m_P L g \sin\alpha \\ 0 \end{bmatrix}; \quad H = \begin{bmatrix} h_{11} & h_{12} & 0 \\ h_{21} & h_{22} & 0 \\ 0 & 0 & h_{33} \end{bmatrix}$$

$$B = \begin{bmatrix} \frac{1}{R} & \frac{1}{R} \\ -1 & -1 \\ -\frac{D}{2R} & \frac{D}{2R} \end{bmatrix}; \quad \tau = \begin{bmatrix} T_L \\ T_R \end{bmatrix}$$

The components of the matrices are specified below: $a_{11} = m_P + 2m_w + \frac{2J_w}{R^2}, a_{12} = a_{21} = m_P L\cos\alpha, a_{22} = I_B + m_p L^2, a_{33} = I_C + 2K + m_w\frac{D^2}{2} + \frac{JD^2}{2R^2} - (I_C - I_A - m_P L^2)\sin^2\alpha, c_{12} = m_P L\dot{\alpha}\sin\alpha, c_{13} = m_P L\dot{\beta}\sin\alpha, c_{23} = (I_C - I_A - m_P L^2)\dot{\beta}\sin\alpha\cos\alpha, c_{31} = m_P L\dot{\beta}\sin\alpha, c_{32} = -(I_C - I_A - m_P L^2)\dot{\beta}\sin\alpha\cos\alpha, c_{33} = -(I_C - I_A - m_P L^2)\dot{\alpha}\sin\alpha\cos\alpha, h_{11} = \frac{2c}{R^2}, h_{12} = h_{21} = -\frac{2c}{R}, \quad h_{22} = 2c, h_{33} = \frac{D^2 c}{2R^2}$.

We divide the entire system into two distinct subsystems: one representing an inverted pendulum system associated with V_{xr} and α, and another governing the TWBMR's heading angle β. The equation (26) can be rewritten as:

$$M\ddot{q} + C\dot{q} + H\dot{q} + G = \begin{bmatrix} \frac{1}{R} & 0 \\ -1 & 0 \\ 0 & 1 \end{bmatrix}\begin{bmatrix} u_1 \\ u_2 \end{bmatrix} \quad (28)$$

where

$$u_1 = T_L + T_R; \quad u_2 = T_R - T_L \quad (29)$$

Therefore, the dynamic equations for α, V_{xr}, and β can be expressed as:

$$\begin{aligned} \ddot{\alpha} &= f_1(x) + g_1(x)u_1 \\ \dot{V}_{xr} &= f_2(x) + g_2(x)u_1 \\ \ddot{\beta} &= f_3(x) + g_3(x)u_2 \end{aligned} \quad (30)$$

3. Control Design

This section primarily aims to maintain the robot's stability while following the target trajectory. The goal is to reduce the associated error vector to zero, represented in the TWBMR's local coordinate frame as:

$$\mathbf{e} = \begin{bmatrix} e_x(t) \\ e_y(t) \\ e_\beta(t) \end{bmatrix} = \begin{bmatrix} \cos\beta & \sin\beta & 0 \\ -\sin\beta & \cos\beta & 0 \\ 0 & 0 & 1 \end{bmatrix}\begin{bmatrix} x_d - x \\ y_d - y \\ \beta_d - \beta \end{bmatrix} \quad (31)$$

where $[x_d; y_d; \beta_d]^T$ represents the target position of the TWBMR.
By differentiating the equation, we obtain:

$$\begin{aligned} \dot{e}_x(t) &= \dot{\beta}e_y - V_{xr} + V_{xrd}\cos e_\beta \\ \dot{e}_y(t) &= -\dot{\beta}e_x + V_{xrd}\sin e_\beta \\ \dot{e}_\beta(t) &= \dot{\beta}_d - \dot{\beta} \end{aligned}$$

where V_{xrd} represents the target linear velocity of the TWBMR along the m_1 axis.

To achieve this regulation, two inner control loops are considered. The first approach employs the backstepping method to guarantee accurate path following by the robot. The following approach consists of two Sliding Mode Controllers (SMCs), aimed at driving the velocities toward their target values and

preserving the robot's stability: A conventional Sliding Mode Controller (SMC) is implemented to regulate the robot's planar angle, producing the control input u_2, while a two-layer fast terminal SMC is employed to manage the tilt angle and linear velocity, generating the control input u_1.

3.1. Backstepping Kinematic Control Design

To accomplish the trajectory tracking, the backstepping technique is used. This method breaks down complex systems into simpler subsystems and offers a clear structure for the controller to bring the errors $\mathbf{e} \to 0$ when $t \to \infty$.

Lemma 1. For all real numbers x,

$$\mu(x) = x \sin(\arctan(x)) \geq 0,$$

Equality is achieved precisely when $x = 0$.

Proof. The scenarios for the cases $x = 0$, $x > 0$, and $x < 0$ were examined separately. In scenario $x = 0$, it's clear that $\mu(x) = 0$; in cases $x > 0$, it follows that $\arctan(x) \in (0, \frac{\pi}{2})$, so $\sin(\arctan(x)) \in (0, 1)$, and $\mu(x) > 0$; and when $x < 0$, we have $\arctan(x) \in \left(-\frac{\pi}{2}, 0\right)$, $\sin(\arctan(x)) \in (-1, 0)$, hence $\mu(x) > 0$.

Consider a scalar function V as a candidate Lyapunov function:

$$V = \frac{1}{2}(e_x^2 + e_y^2) \tag{32}$$

When $e_x = 0$, the Lyapunov function V became

$$V = \frac{1}{2}e_y^2 \tag{33}$$

Then, taking the derivative, we have:

$$\begin{aligned} \dot{V} &= e_y \dot{e}_y \\ &= e_y(-\dot{\beta} e_x + V_{xrd} \sin e_\beta) \\ &= e_y V_{xrd} \sin e_\beta \end{aligned} \tag{34}$$

Let $e_\beta = -\arctan(e_y V_{xrd})$, $\dot{V}$ can be written as:

$$\begin{aligned} \dot{V} &= e_y V_{xrd} \sin\left(-\arctan(e_y V_{xrd})\right) \\ &= -e_y V_{xrd} \sin\left(\arctan(e_y V_{xrd})\right) \end{aligned} \tag{35}$$

Based on Lemma 3.1, $V \leq 0$ is satisfied. Therefore, when e_x converges to 0 and e_β converges to $-\arctan(e_y V_{xrd})$, then e_y also converges to 0 which also leads e_β converges to 0. To achieve that, two Lyapunov functions are characterized as follows:

$$V_1 = \frac{1}{2}e_x^2 \tag{36}$$

$$V_2 = \frac{1}{2}(e_\beta + \arctan(e_y V_{xrd}))^2 \tag{37}$$

The derivation of equation (36) and (37) is represented by the following equation;

$$\dot{V}_1 = e_x \dot{e}_x = e_x(\dot{\beta} e_y - V_{xr} + V_{xrd} \cos e_\beta) \tag{38}$$

$$\begin{aligned} \dot{V}_2 = (e_\beta + \arctan(e_y V_{xrd})) \\ \left(\dot{\beta}_d - \dot{\beta} + \frac{\dot{V}_{xrd} e_y + V_{xrd}^2 \sin(e_\beta) - V_{xrd}\dot{\beta} e_x}{(e_y V_{xr})^2 + 1}\right) \end{aligned} \tag{39}$$

To ensure V_1 and $V_2 \leq 0$, the backstepping kinematic control laws can be introduced as follow:

$$\begin{bmatrix} V_r \\ \dot{\beta}_r \end{bmatrix} = \begin{bmatrix} k_x e_x + \dot{\beta} e_y + V_{xrd} \cos e_\beta \\ \dot{\beta}_d + \dfrac{\dot{V}_{xrd} e_y + V_{xrd}^2 \sin(e_\beta) - V_{xrd}\dot{\beta} e_x}{(e_y V_{xr})^2 + 1} \\ + k_\beta\left(e_\beta + \arctan(e_y V_{xrd})\right) \end{bmatrix} \tag{40}$$

where k_x, k_β are positive constants.
Substituting equations (40) into (39) :

$$\dot{V}_1 = -k_x e_x^2 \tag{41}$$

$$\dot{V}_2 = -k_\beta\left(e_\beta + \arctan(e_y V_{xrd})\right)^2 \tag{42}$$

Therefore it can be concluded that $\dot{V}_1, \dot{V}_2 \leq 0$, so the control law is stable according to the Lyapunov theorem.

3.2. Sliding Mode Control Design

The SMC controller is designed to ensure that V_{xr} and $\dot{\beta}$ converge to V_r and $\dot{\beta}_r$, respectively, while α converges to zero. To achieve this, new error vectors are redefined as follows:

$$\dot{e}_{x1} = V_r - V_{xr} \tag{43}$$

$$e_{\beta 1} = \beta_r - \beta \tag{44}$$

3.2.1. Two-layer Fast Terminal SMC

As mentioned above, the system is divided into two subsystems. One of them is referred to $\dot{V}_{xr}$ and $\ddot{\alpha}$, which is influenced by u_1. The objective of this subsystem is to ensure that V_{xr} converges to V_r as given in (40) and α converges to zero. Considering the structure of the fast terminal sliding mode, a pair of first-layer sliding surfaces for the subsystem is defined as in (45).

$$\begin{aligned} S_x &= \dot{e}_{x1} + c_1 e_{x1} + c_2 e_{x1}^{q1/p1} \\ S_\alpha &= \dot{e}_\alpha + c_3 e_\alpha + c_4 e_\alpha^{q2/p2} \end{aligned} \tag{45}$$

The two-layer sliding surface is formulated as the combination of the two individual surfaces S_α and S_x:

$$S = \zeta S_\alpha + \gamma S_x \tag{46}$$

Consider the overall control input of the sliding-mode controller as defined in (47):

$$u_1 = \frac{1}{\zeta g_1 + \gamma g_2}\left[\zeta\left(-f_1 + c_3 \dot{e}_\alpha + c_4 \frac{q_2}{p_2} \dot{e}_\alpha e_\alpha^{\frac{q_2}{p_2}-1}\right)\right.$$

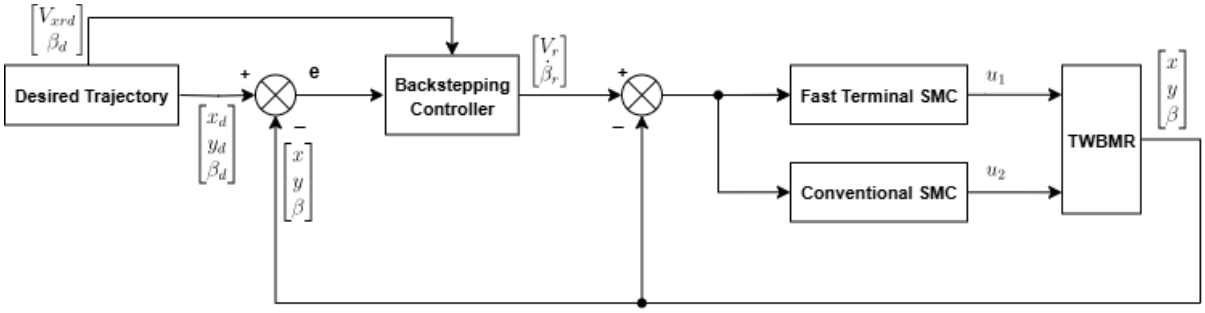

Fig. 2. Control diagram

$$+ \gamma\left(\dot{V}_r - f_2 + c_1\dot{e}_{x1} + c_2\frac{q_1}{p_1}\dot{e}_{x1}e_{x1}^{\frac{q_1}{p_1}-1}\right) + k_1 sign(S) + k_2|S|\Big] \quad (47)$$

where k_1 and k_2 are positive constants. For demonstrating the controller's stability, the following positive definite Lyapunov function is adopted:

$$V = \frac{1}{2}S^2 \quad (48)$$

By differentiating the Lyapunov function with respect to time, we have:

$$\begin{aligned}\dot{V} &= S\dot{S} \\ &= S(-k_1 sign(S) - k_2|S|) \\ &= -k_1|S| - k_2S^2\end{aligned} \quad (49)$$

From (49), the system is guaranteed to be asymptotically stable according to the Lyapunov method. One can conclude that the sliding surface S reaches zero in finite time. This implies that S_α and S_x converge to zero asymptotically.

The convergence times for the system states to reach $S_x = 0$ and $S_\alpha = 0$ are determined as follows:

$$t_x = \frac{p_1}{c_1(p_1 - q_1)}\ln\frac{c_1e_{x1}(0)^{(p_1-q_1)/p_1} + c_2}{c_2} \quad (50)$$

$$t_\alpha = \frac{p_2}{c_3(p_2 - q_2)}\ln\frac{c_3e_\alpha(0)^{(p_2-q_2)/p_2} + c_4}{c_4} \quad (51)$$

When the system state is distant from the equilibrium point, the effect of the linear sliding mode is negligible, and the convergence speed is mainly governed by the nonlinear component.

3.2.2. Conventional SMC Design

From (30), β is influenced by u_2. The objective of this control law is to regulate β to follow the reference β_r in (40). The sliding mode surface is designed as:

$$S_\beta = \dot{e}_{\beta1} + c_5e_{\beta1} \quad (52)$$

The derivative of the sliding surface is given by:

$$\begin{aligned}\dot{S}_\beta &= \ddot{e}_{\beta1} + c_5\dot{e}_{\beta1} \\ &= \ddot{\beta}_r - f_3 - g_3u_2 + c_5\dot{e}_\beta\end{aligned} \quad (53)$$

The following Lyapunov function is chosen:

$$V_\beta = \frac{1}{2}{S_\beta}^2 \quad (54)$$

After taking derivative of V_β we have:

$$\begin{aligned}\dot{V}_\beta &= S_\beta\dot{S}_\beta \\ &= S_\beta(\ddot{\beta}_d - f_3 - g_3u_2 + c_5\dot{e}_{\beta1})\end{aligned} \quad (55)$$

In order to make $\dot{V}_\beta < 0$, the input signal u_2 is chosen as:

$$u_2 = g_3^{-1}(\ddot{\beta}_r - f_3 + c_5\dot{e}_{\beta1} + k_3 sign(S_\beta) + k_4|S_\beta|) \quad (56)$$

Then we have $\dot{V}_\beta = -k_3|S_\beta| - k_4S_\beta^2 < 0$, so S_β and β converge to zero and the system is stable according to the Lyapunov criterion,

3.3. Effect of Controller Parameters

The proposed hybrid controller involves 13 design parameters, which are summarized in Table 1. Although the number of parameters is relatively large, they are not tuned simultaneously. Instead, a hierarchical systematic tuning procedure is employed based on the decoupled structure of the robot dynamics. This approach ensures that the inner-loop stability (balancing) is prioritized before optimizing the outer-loop tracking performance.

Table1 Definition of control parameters and their physical significance

Category	Parameters	Physical Significance
Kinematic	k_x, k_β	Trajectory tracking error convergence
FTSMC Surface	c_1, c_2, c_3, c_4	Finite-time convergence of V_x and α
SMC Surface	c_5	Convergence of heading angle β
Reaching Law	k_1, k_2, k_3, k_4	Robustness against uncertainties
Coupling	γ, ζ	Balance between translational motion and tilt stabilization

To make the tuning process more transparent, the parameter analysis is summarized into four technical remarks using the defined symbols. These remarks highlight the inherent trade-offs among tracking precision (k_x, k_β), balancing stability (c_3, c_4, ζ), and control smoothness (c_1, c_2, k_i).

Remark 1 : Increasing k_x and k_β accelerates the convergence of the tracking errors e_x, e_y, and β. However, excessively large k_x may intensify pitch oscillations due to the underactuated nature of the system. Therefore, k_x is selected to balance tracking performance and allowable pitch motion.

Remark 2 : The sliding surface parameters are selected such that $(c_3, c_4) \gg (c_1, c_2)$. Larger values of c_3 and c_4 enhance the effective stiffness for stabilizing the pitch angle α, while c_1 and c_2 are chosen as very small values to ensure smooth control action and avoid singularity issues near $s = 0$. c_5 balances heading responsiveness and centrifugal disturbance; it must be tuned to allow smooth cornering without compromising the upright stability of the pitch angle α. Too large c_5 causes aggressive turning and pitch instability, while too small c_5 leads to slow response and poor tracking on sharp curves.

Remark 3 : Both (k_1, k_2) and (k_3, k_4) are derived from the Lyapunov-based reaching law, but their effects on the system behavior differ significantly. The gains (k_1, k_2) directly act on the unstable subsystems, namely the balancing and velocity loops, rendering the system highly sensitive to their tuning. In contrast, (k_3, k_4) primarily regulate the heading loop β, which is kinematically stable. Since the heading loop is kinematically stable, these gains primarily affect turning accuracy and the capability to maintain the desired heading in the presence of friction uncertainties. Larger values of k_i enhance steady-state error attenuation and robustness; however, they should be properly bounded to prevent actuator saturation and excessive mechanical loading.

Remark 4 : The coupling factors γ and ζ are selected as small weighting terms $(\gamma, \zeta \ll 1)$ to preserve the dominance of the balancing loop over the velocity control loop. This choice enhances stability when the robot undergoes rapid velocity variations during trajectory tracking.

4. Simulation Results

For this part, to demonstrate the effectiveness of the controller, the proposed control strategies are implemented within the TWBMR dynamic model in MATLAB Simulink. Two simulation driving scenarios are considered: balancing performance with an initial nonzero tilt angle, and movement at constant velocity where the system's starting state does not coincide with the origin of the reference trajectory. The parameters of the TTWBMR used in the simulation are as follows.

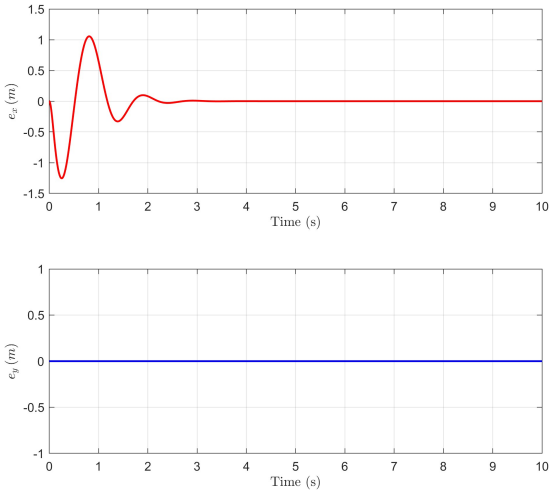

(a) Position error along the x-axis and y-axis

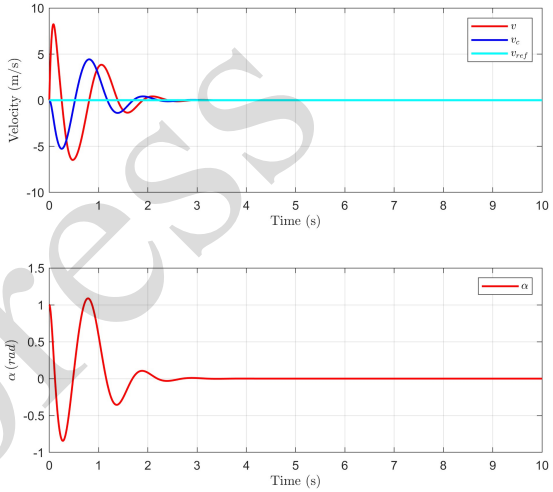

(b) Vehicle velocities and pitch angle

Fig. 3. The results of TWBMR balancing control

The distance between the two wheels is $D = 0.6$ m, and the length of the pendulum is $L = 0.5$ m. Each wheel has a radius of $R = 0.15$ m. The mass of the pendulum body (excluding the wheels) is $m_p = 27$ kg, while the mass of each wheel is $m_w = 2$ kg. The moments of inertia of the wheels are $J = 0.0225\,\text{kg·m}^2$ and $K = 0.015\,\text{kg·m}^2$. For the pendulum, the principal moments of inertia about its center of mass are $I_A = 0.005\,\text{kg·m}^2$, $I_B = 0.005\,\text{kg·m}^2$, and $I_C = 0.002\,\text{kg·m}^2$. The gravitational acceleration is taken as $g = 9.81\,\text{m/s}^2$, and the viscous damping coefficient is $c_\alpha = 0.7$.

4.1. Stability and Tracking Results

In the first simulation scenario, the Two-Wheeled Balancing Mobile Robot (TWBMR) was tested for its self-balancing capability around the upright equilibrium position. The desired tilt angle, linear velocity, and position were all set to zero, while the initial tilt angle was assigned a nonzero value of 1 rad to simulate an initial perturbation. As shown in Fig.3a, the position error along the x-axis initially exhibits an overshoot caused by the corrective motion of the

robot attempting to restore balance. This transient behavior quickly diminishes, and the error converges to zero within approximately 3 s, indicating a fast stabilization response. Since the robot in this case is constrained to move only in the plane, the position error along the y-axis remains zero throughout the simulation, as illustrated in Fig.3a. The evolution of the pitch angle, presented in Fig.3b, further confirms the effective balancing performance of the proposed controller. The tilt angle α decreases smoothly and converges to zero with a minor overshoot of about 0.4 rad, showing both rapid convergence and good damping characteristics without excessive oscillations. This demonstrates that the two-layer FTSMC structure efficiently suppresses the nonlinear coupling between the tilt and translational dynamics. The velocity response shown in Fig.3b exhibits similar stability characteristics: the linear velocity quickly returns to zero once the robot regains its upright position. This implies that the balance recovery and position stabilization occur almost simultaneously, validating the effectiveness of the backstepping–FTSMC-based control design in maintaining equilibrium while minimizing position drift and oscillation.

In the second simulation, the controller performance was evaluated for a combined balancing and trajectory-tracking task. The robot was commanded to follow a straight-line trajectory with a desired constant velocity of 1 m/s. The initial pitch angle was again set to 1 rad, and the starting coordinates were defined as $(-1, -1)$, introducing both position and orientation deviations from the reference path. As illustrated in Fig.4, the proposed hybrid controller successfully enables the robot to follow the desired trajectory while maintaining its self-balancing ability. The position errors along both the x- and y-axes converge rapidly to zero within approximately 3 s, indicating precise trajectory tracking. The tilt angle α remains stable throughout the motion, with a maximum deviation of about 0.5 rad (corresponding to 28.65°), which is quickly compensated by the fast terminal sliding mode mechanism. The velocity response demonstrates smooth convergence toward the reference velocity, with minimal steady-state error and negligible oscillations, confirming the controller's robustness to initial state offsets and system nonlinearities. Overall, these results validate that the proposed backstepping–FTSMC controller provides both fast convergence and strong stability, ensuring accurate path tracking and effective self-balancing under varying initial conditions.

4.2. Robustness Evaluation

To rigorously evaluate the robustness of the proposed Backstepping-FTSMC strategy, additional simulations are conducted by considering external

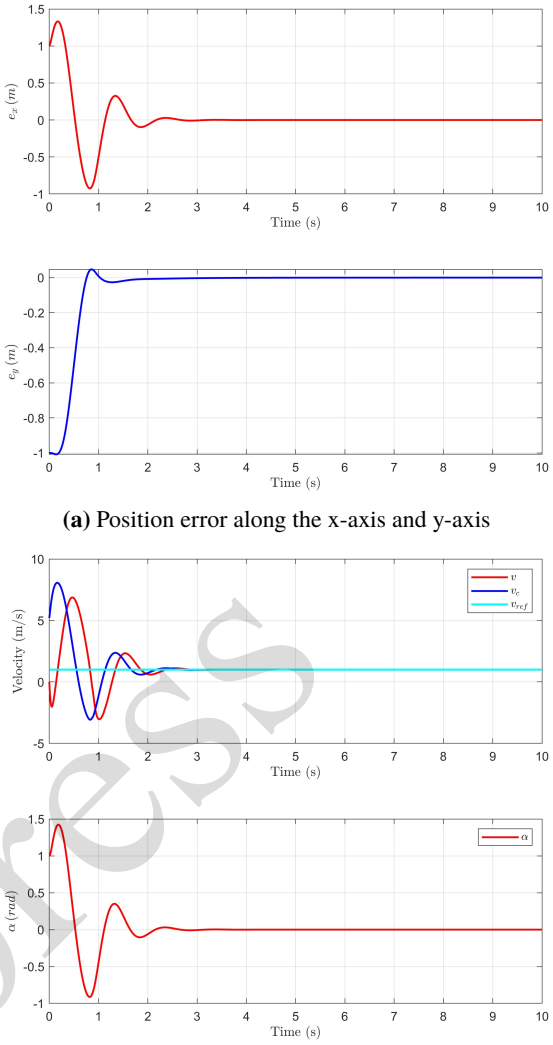

(a) Position error along the x-axis and y-axis

(b) Vehicle velocities and pitch angle

Fig. 4. Simulation results for moving with velocity of 1 m/s

disturbances and model uncertainties. In this robustness evaluation, the following two cases are considered:

*Case 1:*A high-frequency external disturbance modeled as $\Delta f(t) = \sin(40t)$ is added to the system dynamics, while the system parameters remain at their nominal values, as can be seen in Fig.5.

Case 2: In addition to the external disturbance $\Delta f(t) = \sin(40t)$, a model parameter variation is introduced by increasing the pendulum mass from 27 kg to 33 kg. The controller parameters are kept unchanged in both cases, as can be seen in Fig.6.

Under the high-frequency disturbance Fig.5, the tilt angles α and β remain close to their nominal responses. The convergence characteristics are largely preserved, and no noticeable degradation in transient performance is observed. Although the disturbance introduces small oscillatory components in the tracking errors, these remain bounded and do

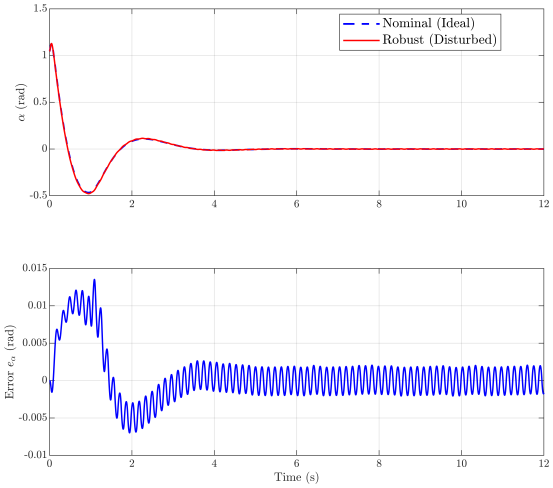

(a) Response of α under high-frequency external disturbance.

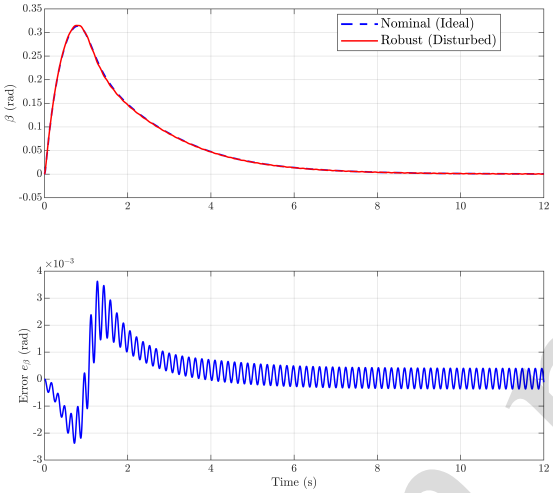

(b) Response of β under high-frequency external disturbance.

Fig. 5. Responses under high-frequency external disturbance

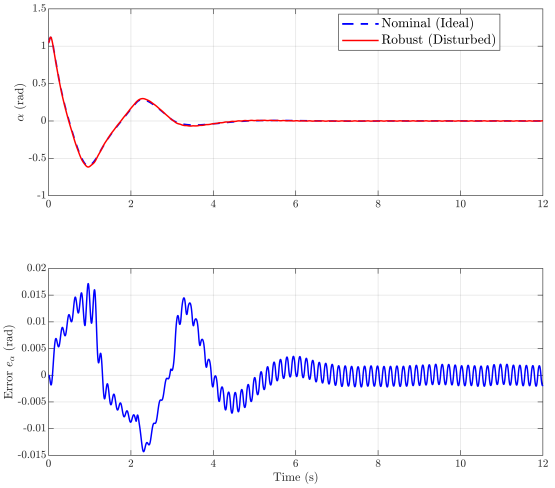

(a) Response of α under combined payload variation and external disturbance.

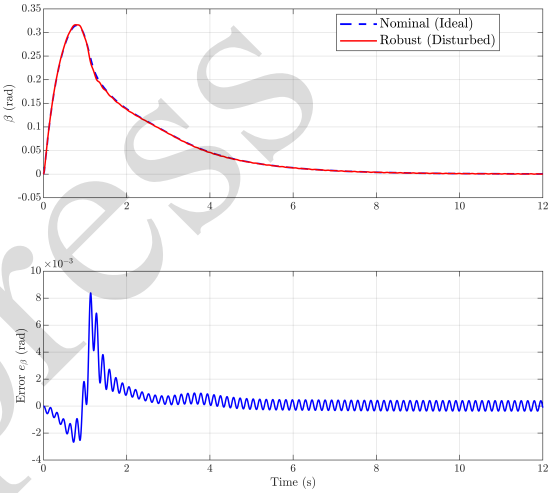

(b) Response of β under combined payload variation and external disturbance.

Fig. 6. Responses under combined payload variation and external disturbance

not compromise stability. This behavior highlights the controller's capability to attenuate high-frequency dynamic uncertainties.

When both external disturbance and payload variation are considered Fig.6, the system continues to exhibit stable and well-damped responses. Despite the increased mass and resulting model mismatch, the tilt angles still converge to the equilibrium point without instability or steady-state offset. W h ile the tracking errors become slightly larger compared to the previous case, they remain bounded, confirming that the controller retains robust performance under combined uncertainties.

4.3. Comparative Simulation Results

A comparative simulation result is presented to evaluate the control performance of the proposed controller in comparison with an HSMC proposed in [17]. To further evaluate the robustness of the proposed control strategy, simulation experiments are conducted by considering the following two cases:

Case 1: Disturbance-Free Condition. In this case, the system operates under nominal conditions without any external disturbance. All model parameters are kept at their nominal values, and the control performance is evaluated as a baseline reference for comparison.

Case 2: External Disturbance. In this case, an external disturbance is introduced into the system dynamics to examine the robustness of the proposed controller. The disturbance is modeled as $f(t) = 0.5\sin(20t)$, representing a bounded, time-varying perturbation acting on the plant, while all other system parameters remain unchanged.

For both cases, the initial conditions of the system are set as $\alpha(0) = 1$ rad and $\beta(0) = \pi/6$ rad. Moreover, the controller parameters are kept identical to ensure a

fair comparison. The simulation results corresponding to these two cases are presented in Fig.7, where the time responses of the tilt angles α and β.

Based on the simulation results in Fig.7a, the proposed FTSMC demonstrates a faster convergence rate than HSMC for all three states x, α, and β. Under FTSMC, the system states reach the vicinity of the reference trajectories in a shorter time, highlighting its finite-time convergence property. Regarding the settling time, both controllers ensure asymptotic stability; however, FTSMC achieves steady-state conditions earlier, particularly for the angular states α and β. Moreover, FTSMC exhibits smaller overshoot and reduced transient oscillations compared to HSMC.

In the presence of the external disturbance $f(t) = 0.5\sin(20t)$, the proposed FTSMC still maintains superior control performance compared to HSMC. As shown in Fig.7b, all system states under FTSMC remain bounded and converge rapidly to their reference trajectories despite the disturbance. Compared with HSMC, FTSMC exhibits stronger disturbance rejection capability, characterized by faster convergence and smaller oscillation amplitudes in the angular states α and β. In particular, the tracking performance of FTSMC is less affected by the high-frequency disturbance, whereas HSMC suffers from more pronounced residual oscillations. These results demonstrate the robustness of the proposed FTSMC against external disturbances.

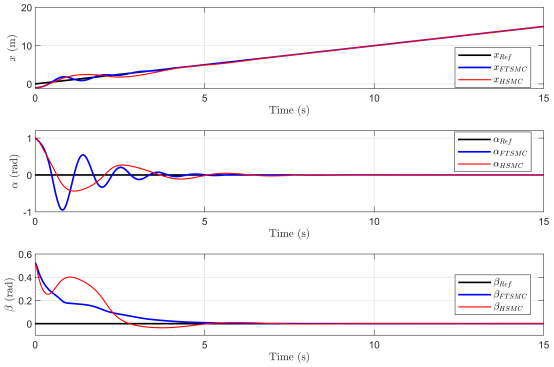

(a) Comparison results under disturbance-free conditions.

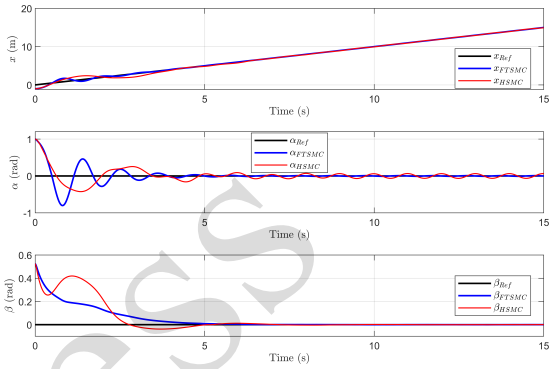

(b) Comparison results under external disturbance.

Fig. 7. Comparison results

5. Conclusion

This study introduced a hybrid control approach that combines Backstepping and FTSMC to achieve both balancing and trajectory tracking for a TWBMR. The dynamic model was established using the Lagrangian method, while the control structure was designed with two layers: the FTSMC ensuring rapid convergence of tilt and velocity errors, and the conventional SMC stabilizing the heading angle. Simulation results verified that the proposed controller provides fast response, strong robustness, and accurate stabilization, with all state errors converging within approximately three seconds and minimal overshoot, confirming its effectiveness in handling nonlinear and underactuated robot dynamics.

is acknowledged that the present study focuses on a simulation-based validation framework, which is a critical step in the early stage of controller design to systematically evaluate stability, convergence properties, and robustness under repeatable conditions. While simulation results provide valuable theoretical insights, experimental validation remains essential to fully assess real-world feasibility and implementation-related challenges. Consequently, future research will focus on experimental validation of the proposed control strategy using a physical TWBMR platform to assess real-world performance under noise and disturbances. the robustness advantages of discontinuous sliding mode control, chattering remains a well-known limitation, especially in real-time implementations with finite s a mpling rates. Practical mitigation strategies, such as boundary-layer techniques, can be employed to smooth the switching action at the expense of a small steady-state tracking error. Alternatively, higher-order sliding mode controllers provide an effective m e ans t o suppress chattering while maintaining high robustness and accuracy. Incorporating these strategies represents a promising direction for future research to improve the practical deployment of the proposed controller. Additionally, adaptive and intelligent extensions of the current controller, such as fuzzy logic, neural networks, or observer-based compensation, will be explored to further enhance robustness against parameter uncertainties and external perturbations. Integrating the control framework into a real-time embedded system will also be pursued to enable practical deployment in robotic applications involving uneven terrain and dynamic environments.

References

[1] N.-L. Tao, D.-H. Pham, M.-k. Pham, and T.-V.-A. Nguyen, Optimization of hierarchical sliding mode control parameters for a two-wheeled balancing mobile robot using the firefly algorithm, Journal of Robotics and Control (JRC), vol. 6, no. 1, pp. 76–88, 2025.

[2] G. Curiel-Olivares, J. Linares-Flores, J. F. Guerrero-Castellanos, and A. Hernández-Méndez, Self-balancing based onactive disturbance rejection controller for the two-in-wheeled electric vehicle, Experimental results, Mechatronics, vol. 76, 2021, Art. no. 102552. https://doi.org/10.1016/j.mechatronics.2021.102552

[3] X. Gao, J. Li, L. Fan, Q. Zhou, K. Yin, J. Wang, C. Song, L. Huang, and Z. Wang, Review of wheeled mobile robots' navigation problems and application prospects inagriculture, IEEE Access, vol. 6, pp. 49248–49268,2018. https://doi.org/10.1109/ACCESS.2018.2868848.

[4] D. Lee, G. Kang, B. Kim, and D. H. Shim, Assistive delivery robot application for real-world postal services, IEEE Access, vol. 9,pp. 141981–141998, 2021. https://doi.org/10.1109/ACCESS.2021.3120618.

[5] D. Wang, H. Leung, A. P. Kurian, K. Hye-Jin, and H. Yoon, A Deconvolutive neural network for speech classification with applications to home service robot, Instrumentation and Measurement, IEEE Transactions on, vol. 59, pp. 3237–3243, Jan. 2011. https://doi.org/10.1109/TIM.2010.2047551.

[6] J. G. Parada-Salado, L. E. Ortega-Garcia, L. F. Ayala-Ramirez, F. J. Perez-Pinal, C. A. Herrera-Ramirez, and J. A. Padilla-Medina, A Low-cost land wheeledautonomous mini-robot for in-door surveillance,IEEE Latin America Transactions, vol. 16,pp. 1298–1305, May 2018. https://doi.org/10.1109/TLA.2018.8407100.

[7] S. Kim and S. Kwon, Dynamic modeling of a two-wheeled inverted pendulum balancing mobile robot, International Journal of Control, Automation and Systems, vol. 13, Aug. 2015. https://doi.org/10.1007/s12555-014-0564-8.

[8] J. R. Rivera-Ruiz, R. Rojas-Galván, J. R. García-Martínez, E. E. Cruz Miguel, and O. A. Barra-Vázquez, Performance evaluation of metaheuristics for LQR controller optimization: A Two-wheel balancing robot case study, IEEE Access, vol. 13, pp. 97870–97888, Jun. 2025. https://doi.org/10.1109/ACCESS.2025.3576343

[9] A. Salerno and J. Angeles, The control of semi-autonomous two-wheeled robots undergoing large payload-variations, in IEEE International Conference on Robotics and Automation, 2004. Proceedings. ICRA '04. 2004, 2004, pp. 1740–1745 Vol.2.

[10] K. Pathak, J. Franch, and S. Agrawal, Velocity and position control of a wheeled inverted pendulum bypartial feedback linearization, IEEE Transactions onRobotics, vol. 21, no. 3, pp. 505–513, 2005. https://doi.org/10.1109/TRO.2004.840905.

[11] Q. Yong, L. Yanlong, X. Zang, and J. Liu, Balance control of two-wheeled self-balancing mobile robot based on TS fuzzy model,in Proceedings of 2011 6th International Forum on Strategic Technology, 2011, pp. 406–409.

[12] Z. Li, Adaptive fuzzy output feedback motion/force control for wheeled inverted pendulums, IET ControlTheory & Applications, vol. 5, pp. 1176–1188, 2011. https://doi.org/10.1049/iet-cta.2010.0176.

[13] D.-H. Pham, M.-K. Pham, M.-L. Nguyen, and T.-V.-A. Nguyen, Type-2 fuzzy control for stabilizing two-wheeled mobile robot under parameter uncertainties, Engineering Research Express, 2025.

[14] Y.-J. Mon, Fuzzy PDC-based LQR sliding neural network control for two-wheeled self-balancing cart, electronics, vol. 14, iss. 9, Apr. 2025, Art. no. 1842. https://doi.org/10.3390/electronics14091842

[15] K. G. Tran, N. H. Nguyen, and P. D. Nguyen, Observer-based controllers for two-wheeled inverted robots with unknown input disturbance and model uncertainty, Journal of Control Science and Engineering, Jul. 2020. https://doi.org/10.1155/2020/7205737

[16] K. G. Tran, T. T. Nguyen, T. Q. Pham, P. D. Nguyen, D. V. Nguyen, and P. A. Nguyen, Control of TWIR using LQR controller and compound disturbance observer,in 2021 Second International Symposium onInstrumentation, Control, Artificial Intelligence, and Robotics (ICA-SYMP), Jan. 2021. https://doi.org/10.1109/ICA-SYMP50206.2021.9358452

[17] H.-N. Le, M.-K. Pham, D.-H. Pham, and T.-V.-A. Nguyen, Trajectory tracking and stabilization of two-wheeled balancing mobile robot with hierarchicaland sliding mode control, International Journal of Dynamics and Control, vol. 13, no. 1, p. 10, 2025.

[18] A. Filipescu, V. Mînzu, B. Dumitrascu, A. Filipescu, and E. Minca, Trajectory-tracking and discrete- time sliding-mode control of wheeled mobile robots, in 2011 IEEE International Conference on Information and Automation, 2011, pp. 27–32.

[19] S. T. Venkataraman and S. Gulati, Control of nonlinear systems using terminal sliding modes, in 1992 American Control Conference, 1992, pp. 891–893.

[20] X. Yu and M. Zhihong, Fast terminal sliding-mode control design for nonlinear dynamical systems, IEEE Transactions on Circuits and Systems I: Fundamental Theory and Applications, vol. 49, no. 2, pp. 261–264,2002. https://doi.org/10.1109/81.983876.

[21] W. Wang, J. Yi, DB. Zha, and XJ. Liu, Double layer sliding mode control for second-order underactuated mechanical systems, Jan. 2005, pp. 3188–3193.

[22] Y. Kanayama, Y. Kimura, F. Miyazaki, and T. Noguchi, A stable tracking control method for an autonomous mobile robot, in Proceedings., IEEE International Conference on Robotics and Automation,vol. 1, pp. 384–389 , 1990.